



NATIONAL TECHNICAL UNIVERSITY OF ATHENS  
School of Naval Architecture and Marine Engineering  
Laboratory of Ship and Marine Hydrodynamics (LSMH)

# **Hydroelastic analysis and optimization of biomimetic propulsion systems with application to ship energy-saving devices**

PhD Thesis

**Dimitra Anevlavi**

*Advisory Committee:*

K. Belibassakis, Professor NTUA (Supervisor)

K.C Giannakoglou, Professor, NTUA

G. Papadakis, Assoc. Professor, NTUA

Athens, 2023





NATIONAL TECHNICAL UNIVERSITY OF ATHENS  
School of Naval Architecture and Marine Engineering  
Laboratory of Ship and Marine Hydrodynamics (LSMH)

# **Hydroelastic analysis and optimization of biomimetic propulsion systems with application to ship energy-saving devices**

PhD Thesis

**Dimitra Anevlavi**

## **Examination Committee:**

1. K. Belibassakis\*, Professor, NTUA (Supervisor)  
School of Naval Architecture and Marine Engineering
2. K.C. Giannakoglou\*, Professor, NTUA  
School of Mechanical Engineering
3. G. Papadakis\*, Associate Professor, NTUA  
School of Naval Architecture and Marine Engineering
4. G.A. Athanassoulis, Emeritus Professor, NTUA  
School of Naval Architecture and Marine Engineering
5. G.S. Triantafyllou, Emeritus Professor, NTUA  
School of Naval Architecture and Marine Engineering
6. S. Voutsinas, Professor, NTUA  
School of Mechanical Engineering
7. V. Riziotis, Associate Professor, NTUA  
School of Mechanical Engineering

\*Member of the Advisory Committee

Athens, 2023





ΕΘΝΙΚΟ ΜΕΤΣΟΒΙΟ ΠΟΛΥΤΕΧΝΕΙΟ

Σχολή Ναυπηγών Μηχανολόγων Μηχανικών

Εργαστήριο Ναυτικής και Θαλάσσιας Υδροδυναμικής (ΕΝΘΥ)

**Υδροελαστική ανάλυση και βελτιστοποίηση  
βιομιμητικών συστημάτων πρόωσης με εφαρμογή σε  
συσκευές εξοικονόμησης ενέργειας πλοίου**

*Διδακτορική Διατριβή της*

**Δήμητρας Ανεβλαβή**

**Εξεταστική Επιτροπή:**

1. Κ. Μπελιμπασσάκης\*, Καθηγητής, ΕΜΠ (Επιβλέπων)  
Σχολή Ναυπηγών Μηχανολόγων Μηχανικών
2. Κ.Χ. Γιαννάκογλου\*, Καθηγητής, ΕΜΠ  
Σχολή Ναυπηγών Μηχανολόγων Μηχανικών
3. Γ. Παπαδάκης\*, Αναπληρωτής Καθηγητής, ΕΜΠ  
Σχολή Ναυπηγών Μηχανολόγων Μηχανικών
4. Γ.Α. Αθανασούλης, Ομότιμος Καθηγητής, ΕΜΠ  
Σχολή Ναυπηγών Μηχανολόγων Μηχανικών
5. Γ.Σ. Τριανταφύλλου, Ομότιμος Καθηγητής, ΕΜΠ  
Σχολή Ναυπηγών Μηχανολόγων Μηχανικών
6. Σ. Βουτσινάς, Καθηγητής, ΕΜΠ  
Σχολή Μηχανολόγων Μηχανικών
7. Β. Ριζιώτης, Αναπληρωτής Καθηγητής, ΕΜΠ  
Σχολή Μηχανολόγων Μηχανικών

\*Μέλη Συμβουλευτικής Επιτροπής

Αθήνα, 2023



Dedicated to my sailing family - you  
have been a constant inspiration.





# Abstract

This is the abstract of my PhD thesis...

Because of the low computational cost and accuracy of the methods described in this work, they are of interest to a range of persons involved in the design, analysis, and optimization of flapping-foil based propulsion systems. The methods can be used in large design-space studies, for which higher-fidelity hydrodynamic or multi-flow simulations are computationally prohibitive.

## Περίληψη στα ελληνικά

Ο Διεθνής Ναυτιλιακός Οργανισμός (IMO) τα τελευταία χρόνια έχει φέρει στο προσκήνιο τις περιβαλλοντικές επιπτώσεις του κλάδου της ναυτιλίας και υιοθετεί μέτρα που αφορούν τη σχεδίαση και λειτουργία πλοίων με στόχο τη μείωση των αερίων ρύπων και την αντιμετώπιση του φαινομένου του θερμοκηπίου [1], [2]. Η μείωση αφορά τις εκπομπές διοξειδίου του άνθρακα ( $CO_2$ ), μεθανίου ( $CH_4$ ), οξειδίων του αζώτου ( $NO_x$ ) και των φθοριούχων αερίων ( $F-Gases$ ) που απαντώνται κυρίως στους τομείς της ψύξης και του κλιματισμού. Τα δύο βασικά μέτρα που έχουν ληφθεί είναι ο σχεδιαστικός δείκτης ενεργειακής απόδοσης (*EEDI*) καθώς και το σχέδιο διαχείρισης της ενεργειακής αποδοτικότητας (*SEEMP*). Με αυτή τη νομοθετική ρύθμιση, οι πλοιοκτήτριες εταιρείες ενθαρρύνονται να λάβουν σοβαρά υπόψη το ενδεχόμενο υιοθέτησης νέων καινοτόμων τεχνολογικών προϊόντων που καθιστούν δυνατή την αναβάθμιση της ενεργειακής απόδοσης των πλοίων.

Υπό το πρίσμα αυτό, η συνεισφορά της έρευνας στον τομέα της υδροδυναμικής βελτιστοποίησης σύγχρονων συστημάτων πρόωσης (συμβατικών και μη), καθώς και η ανάπτυξη τεχνολογίας αξιοποίησης ανανεώσιμης ενέργειας από το θαλάσσιο περιβάλλον στην κατεύθυνση εξοικονόμησης ενέργειας πλοίων κρίνεται απαραίτητη. Ήδη από τις αρχές της δεκαετίας του '90, η μελέτη και σχεδίαση βιομιμητικών προωθητήρων που είναι εμπνευσμένοι από τους μηχανισμούς ώσης και ελιγμών που απαντώνται τόσο στα θαλάσσια θηλαστικά όσο και σε μία οικογένεια ψαριών κεντρίζει το ενδιαφέρον της επιστημονικής κοινότητας [3]. Άλλωστε δεν είναι τυχαίο πως ο αριθμός των δημοσιεύσεων με θέμα την ανάπτυξη υπολογιστικών εργαλείων για την πρόλεξη της ροής γύρω από βιομιμητικά πτερύγια αλλά και η πειραματική μελέτη αυτών έχει πληθύνει σημαντικά τα τελευταία χρόνια. Τα αποτελέσματα είναι ιδιαιτέρως ενθαρρυντικά ενώ καταδεικνύουν πως τα βιομιμητικά πτερύγια μπορούν να παράξουν ώση με βαθμό απόδοσης εξίσου υψηλό με τις ναυτικές έλικες. Επιπλέον, η χαμηλόσυχνη λειτουργία τους, στο τυπικό εύρος αριθμών Strouhal 0.2–0.4 όπου και παρατηρείται η μεγιστοποίηση της απόδοσης, δεν επιβαρύνει το θαλάσσιο περιβάλλον με υψηλά επίπεδα υποθαλάσσιου θορύβου σε αντίθεση τις ναυτικές έλικες. Το γεγονός αυτό καθιστά τα βιομιμητικά συστήματα περισσότερο φιλικά προς το

περιβάλλον [4].

Γνωστά παραδείγματα τεχνολογικών εφαρμογών μη συμβατικών συστημάτων πρόωσης αποτελούν τα ρομποτικά ψάρια *RoboTuna* και *SoFi* του MIT που σχεδιάστηκαν για την εξερεύνηση θαλάσσιου βυθού. Τα υλικά και οι μηχανισμοί ελέγχου που έχουν χρησιμοποιηθεί για την κατασκευή αυτών των προτοτύπων είναι ικανά να προσδώσουν δυνατότητες ενεργητικής και παθητικής παραμόρφωσης στα πτερύγια μεγιστοποιώντας έτσι το βαθμό απόδοσης και προσδίδοντας προηγμένες ελκτικές ικανότητες. Η ανάπτυξη αυτών των προτοτύπων έχει εμπνεύσει πληθώρα συστημάτων βιομιμητικής πρόωσης για μη επανδρωμένα αυτόνομα υποθαλάσσια οχήματα (AUV) [5].

Όσον αφορά τις ναυπηγικές εφαρμογές σε πλοία, διάφορες διατάξεις μη παραμορφούμενων πτερυγίων (σταθερών και μη) έχουν προταθεί κατα καιρούς ως εναλλακτική των ναυτικών ελίκων για το κύριο σύστημα πρόωσης. Η τοποθέτηση ενός παλλόμενου πτερυγίου στη θέση μίας ναυτικής έλικας απαιτεί κοστοβόρες μετασκευές και ενίοτε μία ριζική επανασχεδίαση της περιοχής της πρύμνης. Δεδομένων των δυσκολιών από τεχνολογικής άποψης και πάντοτε σε σχέση με το οικονομικό όφελος της εκάστοτε επένδυσης, η χρήση βιομιμητικών προωθητήρων ως κύριο σύστημα πρόωσης για ποντοπόρα πλοία έχει σχεδόν εγκαταληφθεί, ενώ τη θέση της διαδέχεται η χρήση τους ως συστήματα υποβοήθησης πρόωσης και εξοικονόμησης ενέργειας.

Μία σύγχρονη και καινοτόμα εφαρμογή αποτελεί η μεγάλη κλίμακας συσκευή εξοικονόμησης ενέργειας πλοίου που σχεδιάστηκε και μελετήθηκε από το *SeaTech Consortium* στα πλαίσια ευρωπαϊκού ερευνητικού προγράμματος. Το ταλαντούμενο πτερύγιο τοποθετείται στην πλώρη και αποσβένοντας τις κινήσεις του πλοίου σε κυματισμούς συνεισφέρει με ένα μικρό ποσοστό στην παραγωγή ώσης ενώ ταυτόχρονα μειώνει σημαντικά την αντίσταση του πλοίου σε κυματισμούς, όπως καταδεικνύεται στις εργασίες [6], [7]. Η μείωση αυτή μεταφράζεται σε μειωμένη κατανάλωση καυσίμου, όπου σε συνδυασμό με καινοτομίες στην τεχνολογία του χρησιμοποιούμενου ναυτικού κινητήρα προκύπτει σημαντικό όφελος και ταυτόχρονη μείωση των αέριων ρύπων.

Το αντικείμενο της παρούσας εργασίας αφορά τη μελέτη βιομιμητικών συστημάτων τύπου-ταλαντούμενου-πτερυγίου που παραμορφώνονται παθητικά κάτω από την επίδραση των υδροδυναμικών φορτίσεων. Στόχος είναι η μελέτη των επιδράσεων της ελαστικότητας στην απόδοση των πτερυγίων, καθώς και η ρύθμιση παραμέτρων γεωμετρίας, κίνησης και κατανομής υλικού στην κατασκευή έτσι ώστε οι παραμορφώσεις που θα προκύψουν κατά τη διάρκεια λειτουργίας να επιδρούν θετικά στην απόδοση. Τέτοιες μελέτες βρίσκουν εύρος εφαρμογών στην αεροναυπηγική, με δημοφιλέστερη την κατασκευή πτερυγίων για ανεμογεννήτριες. Ωστόσο, δεδομένου ότι οι τεχνολογικές εφαρμογές παραμορφούμενων πτερυγίων ως συστημάτων υποβοήθησης πρόωσης πλοίου αλλά και ως ανθόρυβων προωθητήρων για μικρά μη επανδρωμένα σκάφη είναι λίγες, η παρούσα εργασία

αποσκοπεί στο να συνεισφέρει με τα ευρήματά της στις προσπάθειες ανάπτυξης βιομηχανικών συσκευών με υψηλούς βαθμούς απόδοσης. Συνοπτική βιβλιογραφική ανασκόπηση περιλαμβάνεται στο [Κεφάλαιο 1](#).

Πιο συγκεκριμένα στα πλαίσια της παρούσας εργασίας, αναπτύχθηκε υπολογιστικό εργαλείο για την αριθμητική προσομοίωση της αλληλεπίδρασης ρευστού με κατασκευή, ικανό να προλέξει τις παθητικές παραμορφώσεις της πτέρυγας προωθητήρα κάτω από υδροδυναμικές και αδρανειακές φορτίσεις. Ιδιαίτερα, η απόκριση των παθητικά παραμορφούμενων πτερυγίων είναι εμμέσως μη-γραμμική καθώς οι παραμορφώσεις (υπό την έννοια αλλαγής σχήματος) επηρεάζουν τα υδροδυναμικά φορτία που αναπτύσσονται στην επιφάνεια του πτερυγίου και αντιστρόφως. Σύμφωνα με τη διεθνή βιβλιογραφία, το νέο υπολογιστικό εργαλείο βασίζεται στην επέκταση και προσαρμογή κωδίκων του Εργαστηρίου Ναυτικής και Θαλάσσιας Υδροδυναμικής, καθώς και την ισχυρή σύζευξη αυτών έτσι ώστε να συνθέσουν έναν υδροελαστικό κώδικα. Τα υπολογιστικά εργαλεία που αναπτύχθηκαν επαληθεύονται μέσω συγκρίσεων με εργασίες από τη διεθνή βιβλιογραφία.

Η κατασκευή της πτέρυγας μοντελοποιήθηκε ως λεπτή πλάκα Kirchhoff-Love, ισότροπου υλικού με πάχος και σταθερά ελαστικότητας (Young's modulus) που μεταβάλλεται κατά το μήκος χορδής της πτέρυγας υπό εξέταση. Η παραδοχή αυτή είναι ικανοποιητική για πτέρυγες με ενδιάμεσους και μικρούς λόγους-επί-μήκους, που απαντώνται κυρίως σε εφαρμογές προωθητήρων μικρών υποθαλάσσιων μη επανδρωμένων σκαφών. Για πτέρυγες με μεγάλο λόγο-επί-μήκους θα μπορούσε να χρησιμοποιηθεί μοντέλο τριδιάστατης δοκού, ωστόσο αυτό προτείνεται για μελλοντική εργασία. Όσον αφορά τη ροή γύρω από την πτέρυγα, μοντελοποιήθηκε με βάση τη θεωρία του ιδανικού (ασυμπίεστου, ατρίβους και μη-συνεκτικού) ρευστού. Για την ανάλυση της απόκρισης της πτέρυγας ως κατασκευή, αναπτύχθηκε κώδικας πεπερασμένων στοιχείων (FEM) με διακριτά στοιχεία πλάκας Kirchhoff (DKT) που προσομοιώνει την κάμψη της πτέρυγας εξαιτίας κατανεμημένου φορτίου πάνω στην επιφάνεια της. Ο υπολογισμός των υδροδυναμικών φορτίσεων προκύπτει ως λύση του μη-μόνιμου υδροδυναμικού προβλήματος.

Πιο συγκεκριμένα, η ροή γύρω από την πτέρυγα μοντελοποιήθηκε με βάση τη θεωρία ιδανικού ρευστού υπό τις παραδοχές ασυμπίεστης, μη-συνεκτικής και αστρόβιλης ροής. Οι εξισώσεις Navier-Stokes κάτω από αυτές τις υποθέσεις απλοποιούνται στην εξίσωση Laplace. Το πρόβλημα αρχικών συνωριακών τιμών που προκύπτει επιλύεται με τη μέθοδο συνωριακών στοιχείων (BEM). Κώδικας του εργαστηρίου επεκτάθηκε στα πλαίσια της εργασίας, έτσι ώστε να μπορεί να διαχειριστεί πτέρυγες που αλλάζουν γεωμετρία κατά τη διάρκεια της κίνησης τους. Ο κώδικας συνωριακών αξιοποιεί τεχνικές παράλληλου προγραμματισμού σε κάρτες γραφικών για την επιτάχυνση των υπολογισμών. Παρόμοιες τεχνικές χρησιμοποιήθηκαν τόσο στον κώδικα πεπερασμένων στοιχείων, όσο και στον

ισχυρά συζευμένο κώδικα (BEM-FEM) που προκύπτει από συγκερασμό των δύο υπολογιστικών εργαλείων.

Στο [Κεφάλαιο 2](#), παρουσιάζεται η μαθηματική μοντελοποίηση του προβλήματος μη μόνιμων ανωστικών ροών γύρω από πτέρυγες που αλλάζουν σχήμα ενεργητικά καθώς και η επίλυση του εν λόγω προβλήματος με τη μέθοδο των συνοριακών στοιχείων. Επαλήθευση του υπολογιστικού εργαλείου πραγματοποιείται μέσω συγκρίσεων με αριθμητικά και πειραματικά αποτελέσματα από τη διεθνή βιβλιογραφία. Στο τέλος του Κεφαλαίου 2 παρουσιάζουμε μελέτες βελτιστοποίησης που αφορούν στη ρύθμιση παραμέτρων γεωμετρίας, κινηματικής και ενεργητικής παραμόρφωσης (active morphing) με στόχο την αύξηση της απόδοσης ενός βιομιμητικού προωθητήρα, που εξετάζεται ως το κύριο σύστημα πρόωσης ενός μικρού υποθαλάσσιου οχημάτος. Τα εξεταζόμενα προφίλ ενεργητικής παραμόρφωσης αφορούν (1) αλλαγές στην κυρτότητα των πτερυγοτομών καθώς και (2) υδροδυναμική συστροφή και κάμψη κατά το εκπέτασμα. Η βέλτιστη ρύθμιση των παραμέτρων παραμόρφωσης στα εξεταζόμενα σενάρια προσδίδει από 9-20% βελτίωση του βαθμού απόδοσης. Τα ποσοστά είναι ιδιαίτερος υψηλά και εν μέρη οφείλονται σε τιμές της γωνίας πρόσπτωσης που κυμαίνεται μεταξύ 10-15 μοιρών. Τα ευρήματα αυτά παρουσιάζονται στο [Κεφάλαιο 2](#) της παρούσας εργασίας. Είναι αρκετά ενθαρρυντικά έτσι ώστε μία πρόταση για μελλοντική εργασία να αποτελεί η πειραματική μελέτη βιομιμητικών πτερυγίων με flap στην περιοχή του χείλους εκφυγής, όπου βρόχος ενεργητικού ελέγχου θα μπορεί να αναλαμβάνει την ενεργητική παραμόρφωση σύμφωνα με τις συνθήκες περιβάλλοντος.

Στο [Κεφάλαιο 3](#),...

Στο [Κεφάλαιο 4](#), παρουσιάζουμε τη σύζευξη των υπολογιστικών εργαλείων στα πλαίσια ανάπτυξης ενός υδροελαστικού κώδικα (BEM-FEM) ικανού να προσομοιώνει με χαμηλό υπολογιστικό κόστος τη ροή γύρω από βιομιμητικούς προωθητήρες (πτέρυγες) γενικής γεωμετρίας που παραμορφώνονται παθητικά (passive morphing) κάτω από υδροδυναμικές και αδρανειακές φορτίσεις. Στη συνέχεια, πραγματοποιήθηκαν επιλύσεις προβλημάτων βελτιστοποίησης όπου η ρύθμιση παραμέτρων γεωμετρίας, κινηματικής και κατανομής υλικούς γίνεται με στόχο τη μεγιστοποίηση της απόδοσης του συστήματος υπό περιορισμούς (λ.χ. δύναμη ώσης). Μελετήθηκε επίσης η επίδραση συνοριακών συνθηκών στην απόδοση της πτέρυγας καθώς εξετάστηκαν διάφορες διατάξεις στήριξης της πτέρυγας, ενώ ελέγχθηκαν διάφορα κριτήρια αντοχής υλικού για την τελική βέλτιστη διάταξη πτέρυγας.

Τέλος, στο [Κεφάλαιο 5](#) παρουσιάζονται συνοπτικά τα επιμέρους συμπεράσματα ευρημάτων της παρούσας διατριβής, ενώ δεν παραλείπονται προτάσεις και κατευθύνσεις μελλοντικής έρευνας.



# Acknowledgments

The present work was supported by the SeaTech Horizon 2020 research and innovation program under grant agreement No 857840 and the Special Account for Research Funding (E.L.K.E.) via the Doctoral Scholarship Program of NTUA. I would also like to acknowledge the financial support I received from the Scholarship Programs of the Bodossaki Foundation and the Society of Naval Architects and Marine Engineers (SNAME), which were valuable to the completion of the present thesis.



# Thanks

I would like to express my sincere gratitude to all the people who supported me through this challenging journey. [Comment: To be added on February.]



# Contents

<b>Abstract</b>	<b>1</b>
<b>Περίληψη στα ελληνικά</b>	<b>2</b>
<b>List of figures</b>	<b>9</b>
<b>List of tables</b>	<b>10</b>
<b>1 Hydromechanics of thin tapered plates</b>	<b>12</b>
1.1 Classical Plate Theory (CPT)	13
1.1.1 Equations of equilibrium	13
1.1.2 Governing equation in terms of deflection	14
1.1.3 Boundary conditions	16
1.2 2D FEM Implementation	17
1.2.1 Global matrix assembly	18
1.2.2 Integration and interpolation	19
1.2.3 Static and dynamic problems	19
1.3 Numerical results and verification	22
1.3.1 Eigenvalues and grid sensitivity	22
1.3.2 Static response	31
1.3.3 Hydrodynamic load excitation	34
1.4 Discussion and future extensions	34
<b>Bibliography</b>	<b>37</b>

# List of Figures

1.1	Nine dof triangular plate bending element. Adapted from ([12])	18
1.2	Unstructured triangulated mesh using Delaunay method. For the $e - th$ triangle we can find the nodal coordinates in $pp$ matrix, and the global numbering of the nodes in $IEN$ (or $tt$ ).	19
1.3	Modal analysis using (a) coarse and (b) fine grid, with black squares indicating the boundary nodes. . . . .	23
1.4	Eigenfunction contour plots for C-C-C-C results from Table 1.2 with color bar referring to the $z$ -coordinate. . . . .	25
1.5	Eigenfunction contour plots for S-S-S-S results from Table 1.3 with color bar referring to the $z$ -coordinate. . . . .	26
1.6	Eigenfunction contour plots for C-F-F-F results from Table 1.2 with color bar referring to the $z$ -coordinate and plate clamped along $x = 0$ . . . . .	27
1.7	Eigenfunction contour plots for C-F-F-F results from Table 1.6 with color bar referring to the $z$ -coordinate. . . . .	30
1.8	Comparison with Navier solution in [18] for S-S-S-S rectangular plate with properties in Table 1.1 under (a) concentrated and (b) uniform load. . . . .	32
1.9	Distributed load scenario. . . . .	33
1.10	Bending displacement [left] and contour [right] for the C-F-F-F plate under distributed load. . . . .	35
1.11	Bending displacement [left] and contour [right] for the F-F-C-F plate under distributed load. . . . .	35

# List of Tables

1.1	Plate properties of thin plate for comparison with [14],[15]. . .	23
1.2	Frequency parameters $\lambda = \omega a^2 \sqrt{\rho h / D}$ for C-C-C-C rectangular plate with constant thickness. . . . .	24
1.3	Frequency parameters $\lambda = \omega a^2 \sqrt{\rho h / D}$ for S-S-S-S rectangular plate with constant thickness. . . . .	24
1.4	Frequency parameters $\lambda = \omega a^2 \sqrt{\rho h / D}$ for C-F-F-F rectangular plate with constant thickness . . . . .	28
1.5	Frequency parameters $\Omega = \omega a^2 \sqrt{\rho_A(h_o) / D(h_o)}$ for C-C-C-C rectangular plate with taper ratio $\tau_x = 0.2$ ( $h_o = 0.01m$ , $h_1 = 0.012m$ ). . . . .	29
1.6	Frequency parameters $\lambda_s = \omega a^2 \sqrt{\rho h_o / D(h_o) / \pi^2}$ for C-F-F-F rectangular plate with taper ratio $\tau_x = 0.5$ ( $h_o = 1.0m$ , $h_1 = 0.5m$ ). [Re-examine] . . . . .	31
1.7	Frequency parameters $\lambda_s = \omega a^2 \sqrt{\rho h_o / D(h_o) / \pi^2}$ for C-C-C-C rectangular plate with taper ratio $\tau_x = 0.25$ ( $h_o = 1.0m$ , $h_1 = 0.75m$ ). [Re-examine] . . . . .	31
1.8	Maximum bending displacement $w_{max}(m)$ for static load cases.	32
1.9	Maximum bending displacement $w_{max}(m)$ for distributed load case. . . . .	34

# Chapter 1

## Hydromechanics of thin tapered plates

The main dimensions of an object under study often dictate the appropriate structural idealisations used for the analysis of the structure, depending also on the application. Typically for wings with relatively high aspect ratios, such as aircraft wings, and applications of aeroelasticity during the preliminary design phase, three-dimensional beams are used to predict the structural response of the wing under load excitation. In this Chapter we focus on the analysis of wings of moderate or low aspect ratios, which can be modelled using a plate idealization, see e.g. the fluid-structure interaction models from Zhu 2017 [8], Dai et al. 2012 [9] and Wang et al. 2020 [8].

In our case, the homogenous and isotropic plate has two identical faces whose dimensions (breadth, length) are considerably greater than the thickness. To account for stiffness variation effects in the context of classical thin plate models, spatial variation of thickness and Young's modulus is introduced.

"The subject of plate bending based on the Kirchhoff and Mindlin plate theories for a variety of transverse loading and boundary conditions has been studied by numerous investigators. The works have been compiled in standard texts on plates such as the ones by Timoshenko and Woinowsky-Krieger (1970), Szilard (1974), Roark and Young (1975), Reismann (1988), Huang (1988), and Reddy (1999a). Closed-form solutions for the stress resultants and deflections have been derived for some plate cases. Where these exact solutions cannot be obtained, the analysts can draw on very general finite element software, such as ABAQUS and COSMOS, to solve their plate bending problems. These software packages for plate analysis usually provide classical (or Kirchhoff) plate theory (CPT) elements and first-order shear deformation (or Mindlin) plate theory (FSDT) elements. The latter type of elements al-

lows for the effect of transverse shear deformation.” from the book by Wang (2000) titled Shear Deformable Beams and Plates.

## 1.1 Classical Plate Theory (CPT)

The Kirchoff (classical) plate theory (CPT) for the case of pure bending is based on the displacement field,

$$u(x, y, z) = -z \frac{\partial w_0}{\partial x} \quad (1.1)$$

$$v(x, y, z) = -z \frac{\partial w_0}{\partial y} \quad (1.2)$$

$$w(x, y, z) = w_0(x, y) \quad (1.3)$$

where  $(u, v, w)$  are the displacement components along the  $(x, y, z)$  coordinate directions, respectively, and  $w_0$  is the transverse deflection of a point on the mid0plane (i.e.,  $z=0$ ). The displacement field in (1.1) implies that straight lines normal to the  $xy$ -plane before deformation remain straight and mornal to the mid-surface after deformation.

### 1.1.1 Equations of equilibrium

The non-zero linear strains associated with the displacement field in Eqs. (1.1) are

$$\epsilon_{xx} = \frac{\partial u}{\partial x} = -z \frac{\partial^2 w_0}{\partial x^2} \quad (1.4)$$

$$\epsilon_{yy} = \frac{\partial v}{\partial y} = -z \frac{\partial^2 w_0}{\partial y^2} \quad (1.5)$$

$$\gamma_{xy} = \left( \frac{\partial u}{\partial y} + \frac{\partial v}{\partial x} \right) = -2z \frac{\partial^2 w_0}{\partial x \partial y} \quad (1.6)$$

$$(1.7)$$

where  $(\epsilon_{xx}, \epsilon_{yy})$  are the normal strains and  $\gamma_{xy}$  is the shear strain. The equilibrium equation is

$$\frac{\partial^2 M_{xx}}{\partial x^2} + 2 \frac{\partial^2 M_{xy}}{\partial x \partial y} + \frac{\partial^2 M_{yy}}{\partial y^2} + q(x, y) = 0, \quad in \quad \Omega_0 \quad (1.8)$$

The thin, constrained theory is very widely used in practice and proves adequate for a large number of structural problems, though, of course, should

not be taken literally as the true behaviour near supports or where local load action is important and is three dimensional, ([10])). [Add schematic diagram for the used sign convention. Typically the z-axis points downwards and the load is positive downwards.] The main reference for this section is the book by ([11]).

### 1.1.2 Governing equation in terms of deflection

$$\sigma_{xx} = \frac{E(x, y)}{1 - \nu^2} (\epsilon_{xx} + \nu \epsilon_{yy}) \quad (1.9)$$

$$\sigma_{yy} = \frac{E(x, y)}{1 - \nu^2} (\epsilon_{yy} + \nu \epsilon_{xx}) \quad (1.10)$$

$$\sigma_{xy} = G(x, y) \gamma_{xy} = \frac{E(x, y)}{2(1 - \nu)} \gamma_{xy} \quad (1.11)$$

where  $E = E(x, y)$  denotes the Young's modulus distribution,  $G = G(x, y)$  the shear modulus distribution, and  $\nu$  Poisson's ratio. Using Eqs. (1.9)-(1.11) and carrying out the indicated integration over the plate thickness, we arrive at

$$\begin{aligned} M_{xx} &= \int_{-h/2}^{h/2} \sigma_{xx} z dz = \frac{E(x, y)}{1 - \nu^2} \int_{-h/2}^{h/2} (\epsilon_{xx} + \nu \epsilon_{yy}) z dz \\ &= -D(x, y) \left( \frac{\partial^2 w_0}{\partial x^2} + \nu \frac{\partial^2 w_0}{\partial y^2} \right) \end{aligned} \quad (1.12)$$

$$\begin{aligned} M_{yy} &= \int_{-h/2}^{h/2} \sigma_{yy} z dz = \frac{E(x, y)}{1 - \nu^2} \int_{-h/2}^{h/2} (\epsilon_{yy} + \nu \epsilon_{xx}) z dz \\ &= -D(x, y) \left( \nu \frac{\partial^2 w_0}{\partial x^2} + \frac{\partial^2 w_0}{\partial y^2} \right) \end{aligned} \quad (1.13)$$

$$\begin{aligned} M_{xy} &= \int_{-h/2}^{h/2} \sigma_{xy} z dz = G(x, y) \int_{-h/2}^{h/2} \gamma_{xy} z dz \\ &= -(1 - \nu) D(x, y) \frac{\partial^2 w_0}{\partial x \partial y} \end{aligned} \quad (1.14)$$

where  $D = D(x, y)$  is the flexural rigidity distribution

$$D(x, y) = \frac{E(x, y) h(x, y)^3}{12(1 - \nu^2)} \quad (1.15)$$

To model properly the geometry of the lifting surface, the plate thickness is provided from the hydrodynamicist as  $h = h(x, y)$ . Also, in the context of

biomimicry, the present CPT formulation takes into account spatial variability of Young's modulus as shown in the expression above. Now, substituting (1.12)-(1.14) to (1.8) yields,

$$\begin{aligned} \frac{\partial^2}{\partial x^2} \left[ D \left( \frac{\partial^2 w}{\partial x^2} + \nu \frac{\partial^2 w}{\partial y^2} \right) \right] + 2(1 - \nu) \frac{\partial^2}{\partial x \partial y} \left[ D \frac{\partial^2 w}{\partial x \partial y} \right] \\ + \frac{\partial^2}{\partial y^2} \left[ D \left( \nu \frac{\partial^2 w}{\partial y^2} + \frac{\partial^2 w}{\partial x^2} \right) \right] + q = 0 \end{aligned} \quad (1.16)$$

The first term in (1.16) can be expanded <sup>1</sup> as follows,

$$\begin{aligned} \frac{\partial^2}{\partial x^2} \left[ D \left( \frac{\partial^2 w}{\partial x^2} + \nu \frac{\partial^2 w}{\partial y^2} \right) \right] &= \frac{\partial}{\partial x} \frac{\partial}{\partial x} \left[ D \left( \frac{\partial^2 w}{\partial x^2} + \nu \frac{\partial^2 w}{\partial y^2} \right) \right] \\ &= \frac{\partial}{\partial x} \left[ \frac{\partial D}{\partial x} \left( \frac{\partial^2 w}{\partial x^2} + \nu \frac{\partial^2 w}{\partial y^2} \right) + D \left( \frac{\partial^3 w}{\partial x^3} + \nu \frac{\partial^3 w}{\partial x \partial y^2} \right) \right] \\ &= \frac{\partial^2 D}{\partial x^2} \left( \frac{\partial^2 w}{\partial x^2} + \nu \frac{\partial^2 w}{\partial y^2} \right) + \frac{\partial D}{\partial x} \left( \frac{\partial^3 w}{\partial x^3} + \nu \frac{\partial^3 w}{\partial x \partial y^2} \right) \\ &\quad + \frac{\partial D}{\partial x} \left( \frac{\partial^3 w}{\partial x^3} + \nu \frac{\partial^3 w}{\partial x \partial y^2} \right) + D \left( \frac{\partial^4 w}{\partial x^4} + \nu \frac{\partial^4 w}{\partial x^2 \partial y^2} \right) \end{aligned} \quad (1.17)$$

The second term in (1.16),

$$2(1 - \nu) \frac{\partial^2}{\partial x \partial y} \left[ D \frac{\partial^2 w}{\partial x \partial y} \right] = 2(1 - \nu) \frac{\partial}{\partial x} \frac{\partial}{\partial y} \left[ D \frac{\partial^2 w}{\partial x \partial y} \right] \quad (1.18)$$

$$\begin{aligned} &= 2(1 - \nu) \frac{\partial}{\partial x} \left[ \frac{\partial D}{\partial y} \frac{\partial^2 w}{\partial x \partial y} + D \frac{\partial^3 w}{\partial x \partial y^2} \right] \\ &= 2(1 - \nu) \left[ \frac{\partial^2 D}{\partial x \partial y} \frac{\partial^2 w}{\partial x \partial y} + \frac{\partial D}{\partial y} \frac{\partial^3 w}{\partial x^2 \partial y} \right. \\ &\quad \left. + \frac{\partial D}{\partial x} \frac{\partial^3 w}{\partial x \partial y^2} + D \frac{\partial^4 w}{\partial x^2 \partial y^2} \right] \end{aligned} \quad (1.19)$$

The third term (1.16) can be expanded as follows,

$$\begin{aligned} \frac{\partial^2}{\partial y^2} \left[ D \left( \nu \frac{\partial^2 w}{\partial x^2} + \frac{\partial^2 w}{\partial y^2} \right) \right] &= \frac{\partial}{\partial y} \frac{\partial}{\partial y} \left[ D \left( \nu \frac{\partial^2 w}{\partial x^2} + \frac{\partial^2 w}{\partial y^2} \right) \right] \\ &= \frac{\partial}{\partial y} \left[ \frac{\partial D}{\partial y} \left( \nu \frac{\partial^2 w}{\partial x^2} + \frac{\partial^2 w}{\partial y^2} \right) + D \left( \nu \frac{\partial^3 w}{\partial y \partial x^2} + \frac{\partial^3 w}{\partial y^3} \right) \right] \\ &= \frac{\partial^2 D}{\partial y^2} \left( \nu \frac{\partial^2 w}{\partial x^2} + \frac{\partial^2 w}{\partial y^2} \right) + \frac{\partial D}{\partial y} \left( \nu \frac{\partial^3 w}{\partial y \partial x^2} + \frac{\partial^3 w}{\partial y^3} \right) \\ &\quad + \frac{\partial D}{\partial y} \left( \nu \frac{\partial^3 w}{\partial y \partial x^2} + \frac{\partial^3 w}{\partial y^3} \right) + D \left( \nu \frac{\partial^4 w}{\partial y^2 \partial x^2} + \frac{\partial^4 w}{\partial y^4} \right) \end{aligned} \quad (1.20)$$

---

<sup>1</sup>Make sure that the differentiation is expressed correctly, one operator at a time using the rules of vector calculus!

Finally the CPT equation for variable flexural rigidity becomes,

$$\begin{aligned} & \Delta \nabla^2 w + \nabla^2 D \nabla^2 w + 2 \nabla D \cdot \nabla (\nabla^2 w) \\ & - (1 - \nu) (\partial_{xx} D \partial_{yy} w - 2 \partial_{xy} D \partial_{xy} w + \partial_{yy} D \partial_{xx} w) = q \end{aligned} \quad (1.21)$$

Or in a more compact form using the following identity from vector calculus

$$\begin{aligned} \nabla^2 (D \nabla^2 w) &= \nabla \cdot \nabla (D \nabla^2 w) = \nabla \cdot (\nabla D \nabla^2 w + D \nabla \cdot (\nabla^2 w)) \\ &= \nabla^2 D \nabla^2 w + \nabla D \cdot \nabla (\nabla^2 w) + \nabla D \cdot \nabla (\nabla^2 w) + D \nabla^4 w \\ &= D \nabla^4 w + \nabla^2 D \nabla^2 w + 2 \nabla D \cdot \nabla (\nabla^2 w) \end{aligned} \quad (1.22)$$

This fourth-order partial differential equation (pde) along with a set of boundary conditions can be used to perform modal analysis and to predict the eigenmodes/eigenfunctions of the system. On the other hand, to produce the weak formulation for finite element analysis it is quite tedious to start from the pde, and therefore it is typical to begin from a hamiltonian principle. Here we also follow this approach, and more details can be found in the next section.

### 1.1.3 Boundary conditions

In our formulation, the plate is symmetric with respect to the  $xz$ -plane and fully submerged within the liquid medium. The side faces of the plate are free from loading, whereas displacements and slopes are zero at the support configuration in the vicinity of the axis of symmetry. This configuration is responsible for transmitting the enforced rigid-body motions to the plate as a whole. [\[Add schematic figure for the plate geometry.\]](#)

Conditions enforced on the primary variables (i.e., generalized displacements:  $w_0$ ,  $\partial w_0 / \partial n$ ) constitute essential (or geometric) boundary conditions, whereas conditions enforced on the secondary variables (i.e., generalized forces  $V_n$ ,  $M_{nn}$ ) constitute natural (or force) boundary conditions.

- At a **free edge**, which is not geometrically restrained in any way, the generalized displacements of the mid-plane are not equal to zero,

$$w_0 \neq 0, \quad \frac{\partial w_0}{\partial n} \neq 0 \quad (1.23)$$

However, the edge may have applied forces and/or moments

$$V_n = Q_n + \frac{\partial M_{ns}}{\partial s} = \hat{V}_n, \quad M_{nn} = \hat{M}_{nn} \quad (1.24)$$

where quantities with a hat are specified forces/moments. For free rectangular plates,  $M_{ns} = 0$ ; hence no corner forces are developed.  $V_n$  is the effective shear force



- A **fixed** (or **clamped**) edge is fully geometrically restrained,

$$w_0 = 0, \quad \frac{\partial w_0}{\partial n} = 0 \quad (1.25)$$

Therefore, the forces and moments on a fixed edge are not known a priori (i.e., they are reactions to be determined as a part of the analysis). For clamped rectangular plates,  $M_{ns} = 0$ , hence no corner forces are developed.

- At a **simply supported** edge,

$$w_0 = 0, \quad M_{nn} = \hat{M}_{nn} \quad (1.26)$$

where  $\hat{M}_{nn}$  is the applied normal bending moment on the edge. For simply supported rectangular plates, a reacting force of  $2M_{ns}$  is developed at each corner of the plate.

## 1.2 2D FEM Implementation

We have developed a finite element code written in *C/C++* with Matlab as the pre- and post-processor. The mesh is generated using Matlab PDE Toolkit Delaunay triangulation (DT) routine.

Determination of suitable shape functions for the plate equation is now much more complex than those needed for  $C^0$  continuity or for beams. The problem of thin plates is associated with fourth-order differential equations leading to a potential energy function which contains second derivatives of the unknown function, thus the shape functions need to be characterized by  $C^1$  continuity.

The main reference for this discussion can be found in Chapter 11 of the book by ([10]). What is the difference between *conforming* and *non-conforming* elements? **Non-conforming** elements: independent interpolation of rotations  $\partial w_0 / \partial n$  and displacement  $w_0$ , imposing continuity as a special constraint, often applied at discrete points only. In this work we use the Discrete Kirchhoff triangle (DKT) with 9 dofs and 3 nodes. This approach is known as a mixed formulation.

Non-conforming methods for  $C^1$  (Hermite element not feasible on triangular mesh). Discrete elements. Mass matrix.

It was then realized that it is impossible to formulate a compatible triangular element with 9 dof with a single-field polynomial expansion for  $w$ .

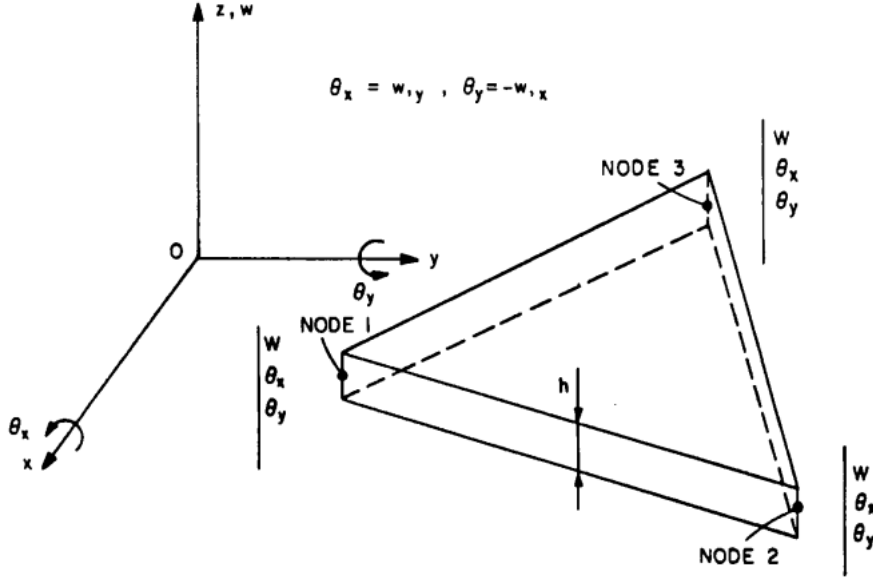


Figure 1.1: Nine dof triangular plate bending element. Adapted from ([12])

### 1.2.1 Global matrix assembly

The mesher provides all relevant information regarding the properties of each triangle and its neighbours, for the generated unstructured mesh. Each triangle is characterized by three nodes and nine degrees-of-freedom are assigned to it (three per node).

First, the element nodal data array – which relates local to global node numbers – is defined as

$$IEN(a, e) = A \quad (1.27)$$

in which  $a$  is the local node number,  $e$  is the element number, and  $A$  is the global node number. The dimensions of  $IEN$  are  $M = 3$ ,  $N = N_{elem}$ . The destination array is defined as

$$ID(i, A) = P \quad (1.28)$$

in which  $i$  the local dof number and  $P$  is the global equation number. Finally, the location matrix is defined as

$$LM(k, e) = ID(i, IEN(a, e)) \quad (1.29)$$

where  $k$  is an index from 1 – 9, since  $LM$  has dimensions  $M = 9$ ,  $N = N_{elem}$ . It is important to note that for the new version of the FEM code, written in C the matrix indices start from 0, whereas in the original version written in Matlab the indices start from 1.

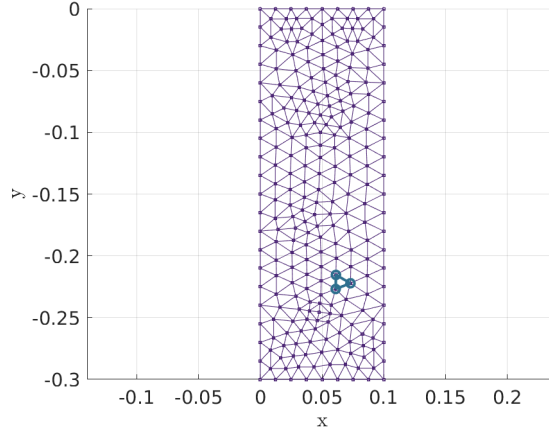


Figure 1.2: Unstructured triangulated mesh using Delaunay method. For the  $e - th$  triangle we can find the nodal coordinates in  $pp$  matrix, and the global numbering of the nodes in  $IEN$  (or  $tt$ ).

### 1.2.2 Integration and interpolation

In practice, most of the integrals (encountered frequently) either cannot be evaluated analytically or the evaluations are very lengthy and tedious. Thus, for simplicity numerical integration methods are preferred and the methods extensively employ the Gaussian quadrature technique that was originally designed for one dimensional cases and the procedure naturally extends to two and three-dimensional rectangular domains according to the notion of the Cartesian product. Gaussian quadratures are considered as the best method of integrating polynomials because they guarantee that they are exact for polynomials less than a specified degree.

Interpolation is performed using the Shepard method for scattered data. [Add++]

### 1.2.3 Static and dynamic problems

The structural governing equation residuals in discretized form can be written as,

$$\{\mathbf{M}\} \frac{d^2 \mathbf{q}}{dt^2} + \{\mathbf{C}\} \frac{d \mathbf{q}}{dt} + \{\mathbf{K}\} \mathbf{q} = \{\mathbf{F}(\mathbf{t})\} \quad (1.30)$$

where  $q$  is the vector of structural displacements and rotations,  $\{\mathbf{M}\}$  is the linear structural mass matrix,  $\{\mathbf{K}\}$  is the stiffness matrix,  $\{\mathbf{C}\}$  is a Rayleigh damping matrix, and  $\{\mathbf{F}\}$  is the hydrodynamic load vector. The *rhs* corresponding to the loading vector is time-varying, whereas the vector of un-

knowns is  $\mathbf{q} = \{w^i, b_x^i, b_y^i\}$ , with  $i$  is the total number of nodes in the triangular mesh on the mid-surface of the plate.

### Time integration

We can produce an equivalent system of first order equations by setting

$$\mathbf{u} = \begin{bmatrix} \dot{\mathbf{q}} \\ \mathbf{q} \end{bmatrix} \quad (1.31)$$

and bring the dynamic equation into the form

$$\begin{bmatrix} \{\mathbf{M}\} & 0 \\ 0 & \{\mathbf{I}\} \end{bmatrix} \cdot \dot{\mathbf{u}} + \begin{bmatrix} \{\mathbf{C}\} & \{\mathbf{K}\} \\ -\{\mathbf{I}\} & 0 \end{bmatrix} \cdot \mathbf{u} = \begin{bmatrix} \{\mathbf{F}\} \\ 0 \end{bmatrix} \quad (1.32)$$

where  $\{\mathbf{I}\}$  is the identity matrix.

**Forward Euler** Assuming that we have the equation in the form  $\dot{\mathbf{u}} = \mathbf{f}(t, \mathbf{u}(t))$  and a time step  $h$  then,

$$\mathbf{u}_{n+1} = \mathbf{u}_n + h\mathbf{f}(t_n, u_n) \quad (1.33)$$

### Implicit (Backward) Euler

$$\mathbf{u}_{n+1} = \mathbf{u}_n + h\mathbf{f}(t_{n+1}, u_{n+1}) \quad (1.34)$$

### Crank-Nicolson

$$\mathbf{u}_{n+1} = \mathbf{u}_n + \frac{1}{2}h\left(\mathbf{f}(t_n, u_n) + \mathbf{f}(t_{n+1}, u_{n+1})\right) \quad (1.35)$$

However, if we do not wish to reduce the second-order system of equations we can implement the following method.

### Newmark Method

$$\dot{\mathbf{q}}_{n+1} = \dot{\mathbf{q}}_n + (1 - \gamma)h\ddot{\mathbf{q}}_n + \gamma h\ddot{\mathbf{q}}_{n+1} \quad (1.36)$$

$$\mathbf{q}_{n+1} = \mathbf{q}_n + h\dot{\mathbf{q}}_n + h^2\left(\frac{1}{2} - \beta\right)\ddot{\mathbf{q}}_n + h^2\beta\ddot{\mathbf{q}}_{n+1} \quad (1.37)$$

where  $\gamma, \beta$  are quadrature parameters; typical values include  $\gamma = 1/2$ ,  $\beta = 1/6$  (linear interpolation) and  $\gamma = 1/2$ ,  $\beta = 1/4$  (averaging). To implement

the Newmark Method we write the dynamic equation for  $t_{n+1}$  and substitute the equations above to produce,

$$\begin{aligned} \left[ \{\mathbf{M}\} + \gamma h \{\mathbf{C}\} + \beta h^2 \{\mathbf{K}\} \right] \ddot{\mathbf{q}}_{n+1} = \{\mathbf{F}\}_{n+1} - \{\mathbf{C}\} \left[ \dot{\mathbf{q}}_n + (1 - \gamma) h \ddot{\mathbf{q}}_n \right] \\ - \{\mathbf{K}\} \left[ \mathbf{q}_n + h \dot{\mathbf{q}}_n + h^2 \left( \frac{1}{2} - \beta \right) \ddot{\mathbf{q}}_n \right] \end{aligned} \quad (1.38)$$

For the numerical implementation,

- if the time step  $h$  is uniform, then  $\{\mathbf{M}\} + \gamma h \{\mathbf{C}\} + \beta h^2 \{\mathbf{K}\}$  can be factored once
- solve the above system of equations for  $\ddot{\mathbf{q}}_{n+1}$
- substitute the result into the expressions in Eqs. (1.36-1.37) for the velocity and displacement respectively.

This method requires initial conditions for the acceleration, velocity and displacement  $\ddot{\mathbf{q}}_n$ ,  $\dot{\mathbf{q}}_n$ ,  $\mathbf{q}_n$  at the first time step. Also the forcing of the future time step is needed. In our case,

1. If the forcing at the first time step is zero, then we need to produce an estimate for the acceleration using Eq. (1.38). This happens only at the first time step.

## Rayleigh damping

COMMENT: Can I find a plate/shell model that uses more advanced damping terms? Tuning Rayleigh coefficients its very time-consuming.

Classical Rayleigh damping is viscous damping which is proportional to a linear combination of mass and stiffness. The damping matrix  $\mathbf{C}$  is given by

$$\mathbf{C} = \alpha \mathbf{M} + \beta \mathbf{K} \quad (1.39)$$

where  $\mathbf{M}$  and  $\mathbf{K}$  are the mass and stiffness matrices respectively and  $\alpha, \beta$  are constants of proportionality. One of the less attractive features of Rayleigh damping however is that the achieved damping ratio  $\xi$  varies with response frequency. The stiffness proportional term contributes damping that is linearly proportional to response frequency and the mass proportional term contributes damping that is inversely proportional to response frequency.

In the 2D version of the FSI code we have two options:

- Use the frequencies from the experiments of Paraz et al. [13] and damping ratio for the first and the third eigenfrequency.
- Use the in vacuo eigenfrequencies from the fem solver and damping ratio to produce the damping coefficients.

In the Paraz et al. [13] experiments we can observe a second peak in the response of the plate. If high values of the stiffness proportional damping coefficient are used this peak is over-damped. Therefore, fine tuning with these experiments means that  $a > b$ . The damping coefficients are characteristic for each material, thus the same damping coefficients shouldn't be used for both plastic and metallic materials for example.

## 1.3 Numerical results and verification

The plateFEM source code is written in C/C++ using LAPACK, BLAS libraries. All computations are performed in an AMD Ryzen 9 3900XT workstation equipped with an NVIDIA GeForce RTX 3080 (10GB VRAM).

Regarding the boundary condition symbolism, for example SS-C-SS-F will identify a rectangular plate with the edges  $x = 0$ ,  $y = 0$ ,  $x = a$ ,  $y = b$  having simply-supported, clamped, simply-supported, and free boundary conditions, respectively.

For the analysis of tapered plates, thickness is assumed constant on each DKT element and Shepard's interpolation with parameter  $p = 2.55$  is used to assign thickness values to each element based on scattered thickness data.

### 1.3.1 Eigenvalues and grid sensitivity

**Rectangular plates with constant thickness.** In Leissa [14] comprehensive and accurate analytical results concerning the free vibration problem of rectangular plates with constant thickness based on the CPT model. All possible combinations (21) of clamped, simply-supported, and free edge conditions are considered, suggesting that this work is indeed a standard reference for benchmarking in the field.

Verification of the FEM begins with comparisons against the closed-form solutions for the free vibration problem of an isotropic, homogeneous rectangular plate with constant thickness. The following boundary conditions are considered: clamped along edges (C-C-C-C), simply supported along edges (S-S-S-S), all edges clamped and all other edges free from loading (C-F-F-F).

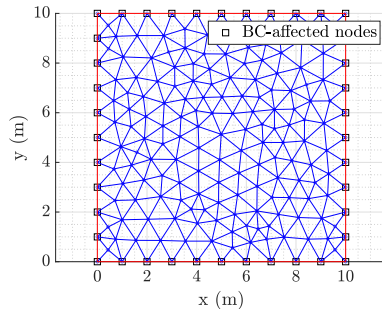
The completely clamped and simply-supported cases are frequently used as a test problem for analytical methods because of the simplicity of the

boundary conditions. The cantilever plate case is included in the benchmarking since it is linked directly to technological applications involving lifting and stabilizing surfaces in the marine and aerospace industries. Table 1.1 summarizes the benchmark parameters. The comparison is performed with respect to the frequency parameter  $\lambda = \omega a^2 \sqrt{\rho/D}$ , thus the plate properties are included to support that this study case lies within the assumptions of thin plate theory for  $a/h \leq 0.1$ .

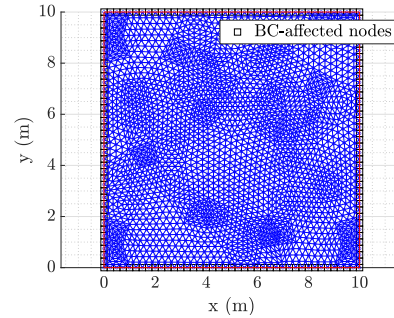
Modal analysis using the plateFEM solver is performed using coarse and fine meshes to obtain additional information regarding grid sensitivity and convergence. The results for all meshes, i.e.  $N_{elem} = \{334, 1336, 5344\}$ , are summarized in Tables 1.2-1.4 for then thin plate benchmark case. The modal frequencies obtained via numerical computations are arranged in ascending order. The coarse and fine grids are provided in Figure 1.3.

Table 1.1: Plate properties of thin plate for comparison with [14],[15].

Material properties		Geometry	
Young's modulus	$E = 210GPa$	dimensions	$a = b = 10m$
Poisson's ratio	$\nu = 0.3$	thickness	$h = 0.01m$
density	$\rho = 7850kg/m^3$	aspect ratio	$a/b = 1$
surface-density ( $\rho_A = \rho h$ )	$\rho_A = 78.5kg/m^2$	thickness/chord	$h/a = 0.001$



(a)  $N_{elem} = 334$



(b)  $N_{elem} = 5344$

Figure 1.3: Modal analysis using (a) coarse and (b) fine grid, with black squares indicating the boundary nodes.

The comparison between the present finite element model and the analytic solutions from Leissa [14] suggest that our DKT solver is capable of predicting the eigenfrequencies with good accuracy as shown in Tables 1.2-1.4.

The accuracy improves for finer mesh discretizations as expected, ensuring grid convergence. In Tables 1.2-1.3 the intermediate mesh discretization with  $N_{elem} = 1336$  the accuracy is of the order of 1.0%, whereas for the fine grid with  $N_{elem} = 5344$  an accuracy of 0.2% is achieved. The results shown that accuracy depends both on the discretization and boundary conditions.

Table 1.2: Frequency parameters  $\lambda = \omega a^2 \sqrt{\rho h / D}$  for C-C-C-C rectangular plate with constant thickness.

id	Leissa [14]	DKT (334)	Diff(%)	DKT (1336)	Diff(%)	DKT (5344)	Diff(%)
1	35.992	36.0121	-0.0558	35.9927	-0.0019	35.9870	0.0139
2	73.413	73.6732	-0.3544	73.4735	-0.0824	73.4138	-0.0011
3	73.413	73.6961	-0.3856	73.4812	-0.0929	73.4159	-0.0040
4	108.27	109.1788	-0.8394	108.4826	-0.1964	108.2833	-0.0123
5	131.64	132.9158	-0.9692	131.9773	-0.2562	131.6832	-0.0328
6	132.24	134.8479	-1.9721	132.9123	-0.5084	132.3826	-0.1078

Table 1.3: Frequency parameters  $\lambda = \omega a^2 \sqrt{\rho h / D}$  for S-S-S-S rectangular plate with constant thickness.

id	Leissa [14]	DKT (334)	Diff(%)	DKT (1336)	Diff(%)	DKT (5344)	Diff(%)
1	19.7392	19.8320	-0.4701	19.7626	-0.1185	19.7451	-0.0299
2	49.3480	49.8485	-1.0142	49.4771	-0.2616	49.3804	-0.0657
3	49.3480	49.9212	-1.1615	49.4947	-0.2973	49.3847	-0.0744
4	78.9568	80.5741	-2.0483	79.3722	-0.5261	79.0610	-0.1320
5	98.6960	100.6417	-1.9714	99.2081	-0.5189	98.8250	-0.1307
6	98.6960	101.5332	-2.8747	99.4196	-0.7332	98.8773	-0.1837

This is evident from Table 1.4 where the fine mesh yields an accuracy of the order of 0.70%. The C-F-F-F boundary conditions are considered more demanding than the fully-clamped case.

Eigen-function contour plots are provided for completeness in Figures 1.4-1.6 for all the examined boundary conditions. Each mode is accompanied by a color bar referring to the bending deformation  $w$  in the  $z$ -axis. These benchmarks verifies that stiffness and mass matrices are implemented correctly in the code.



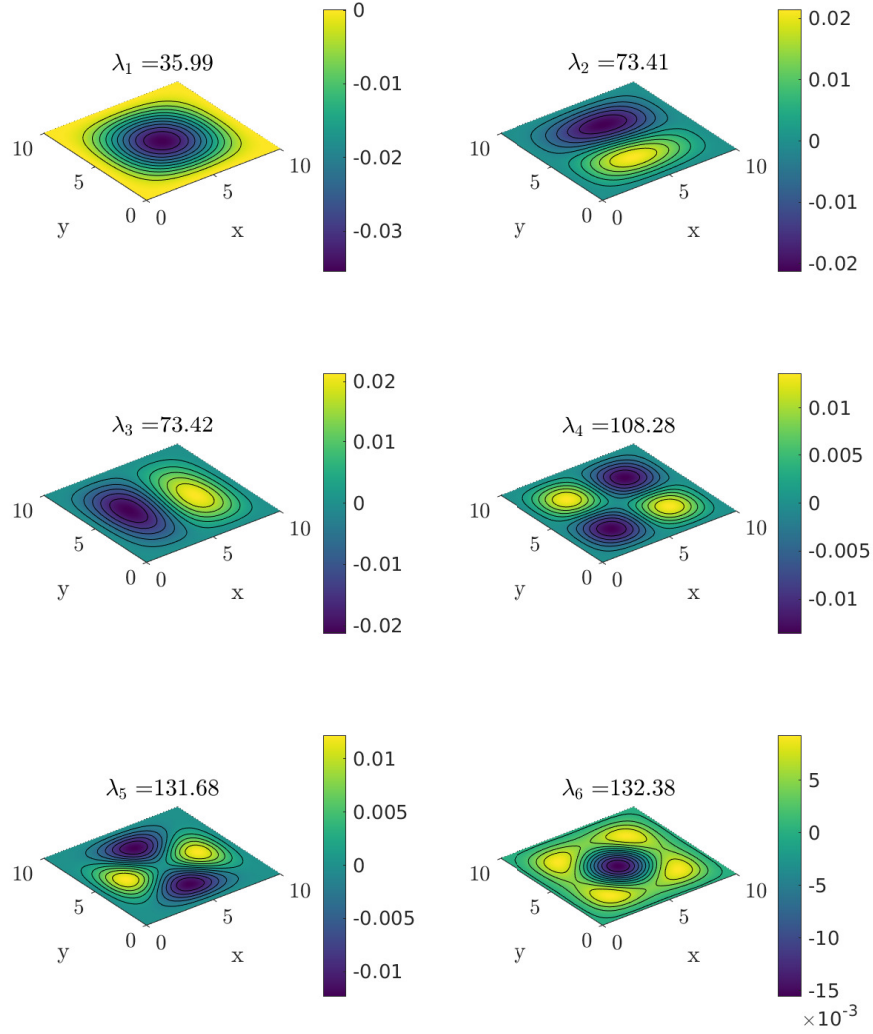


Figure 1.4: Eigenfunction contour plots for C-C-C-C results from Table 1.2 with color bar referring to the  $z$ -coordinate.

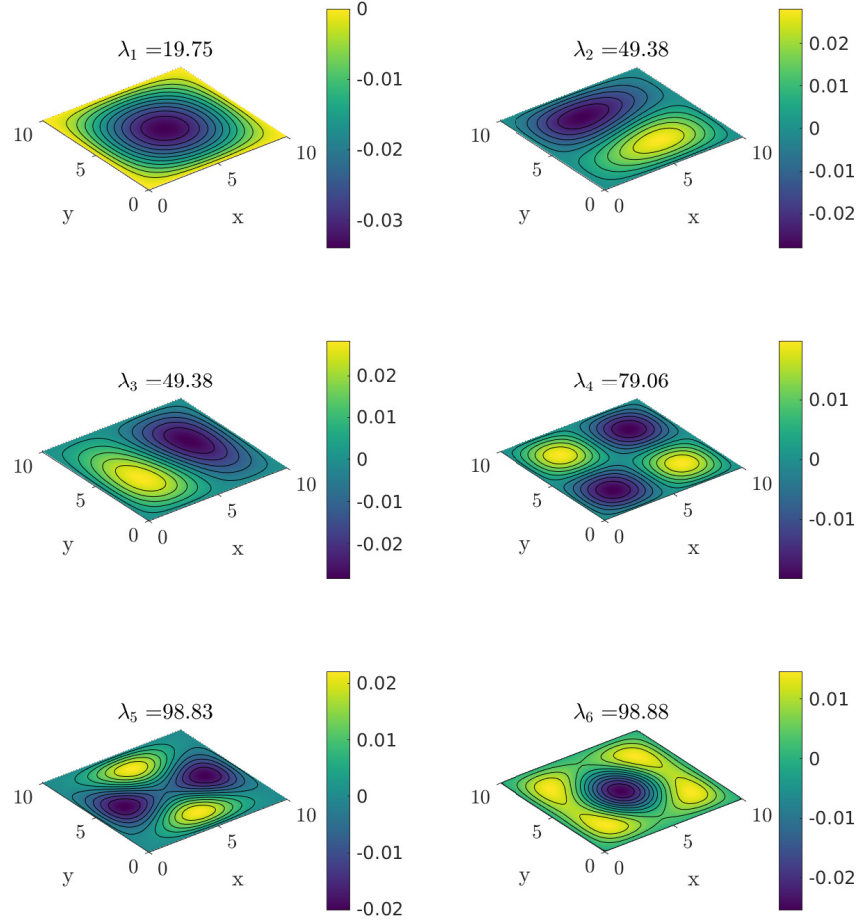


Figure 1.5: Eigenfunction contour plots for S-S-S results from Table 1.3 with color bar referring to the  $z$ -coordinate.

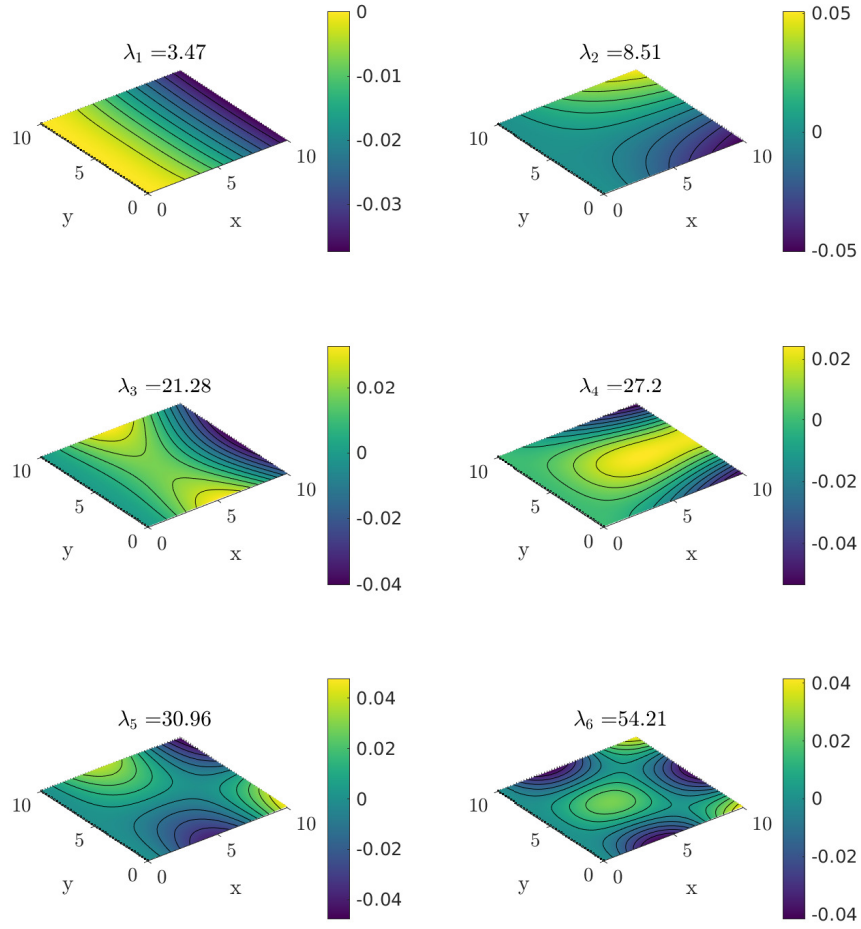


Figure 1.6: Eigenfunction contour plots for C-F-F-F results from Table 1.2 with color bar referring to the  $z$ -coordinate and plate clamped along  $x = 0$ .

Table 1.4: Frequency parameters  $\lambda = \omega a^2 \sqrt{\rho h / D}$  for C-F-F-F rectangular plate with constant thickness

id	Leissa [14]	DKT (334)	Diff(%)	DKT (1336)	Diff(%)	DKT (5344)	Diff(%)
1	3.4917	3.4674	0.6959	3.4702	0.6157	3.4708	0.5986
2	8.5246	8.4045	0.2358	8.5059	0.2194	8.5062	0.2158
3	21.429	21.2803	0.6939	21.2835	0.6790	21.2838	0.6776
4	27.331	27.1772	0.5627	27.1947	0.4987	27.1977	0.4877
5	31.111	31.0194	0.2944	30.9730	0.4436	30.9590	0.4886
6	54.443	54.6274	-0.3387	54.3050	0.2535	54.2140	0.4206

**Rectangular plates with linearly varying thickness.** In Katsikadelis & Sapountzakis [15] results concerning the free vibration of linearly tapered plates along the  $x$ -axis based on a boundary element method are presented. The thickness profile in SI units is defined as,

$$h(x, y) = h_o(1 + \tau_x \frac{x}{a}), \quad x \in [x_o, x_1] = [0, a]. \quad (1.40)$$

where  $\tau_x = h_1/h_o - 1$  denotes the taper ratio and  $h_o = h(0, y)$ ,  $h_1 = h(a, y)$  are known values. Based on the above profile, the thickness along  $x = 0$  is less than thickness along  $x = a$ , i.e.  $h_o < h_1$ .

The case of a fully-clamped plate with properties based on Table 1.1 is selected for comparison. Table 1.5 contains frequency parameter results obtained from the present method and compared against Katsikadelis & Sapountzakis [15] and Kuttler et al. [16]. The latter consists of a finite element model based on the CPT with which our predictions are in very good agreement (0.3% accuracy).

The deviations observed regarding the comparison against Katsikadelis & Sapountzakis [15] results are more evident in higher frequencies and can be attributed to their numerical implementation using boundary elements. It is important to note that results in [15] deviate (up to 3.95%) from the analytic solution in Leissa [14] for C-C-C-C thin rectangular plates with constant thickness. Since, our method is in excellent agreement (0.1% accuracy) with Leissa [14] for this standard case as shown in Table 1.2, the deviations observed for the linearly tapered case are justified.

Regarding the C-F-F-F rectangular plate with linear taper in the  $x$ -axis, relevant results are also presented in Shufrin & Eisenberger [17]. The thick-

ness profile along the  $x$ -axis in their study is based on,

$$h(x, y) = h_o(1 - \tau_x \frac{x}{a}), \quad x \in [x_o, x_1] = [0, a]. \quad (1.41)$$

where  $\tau_x$  denotes the taper ratio. Based on the above profile  $h_o > h_1$ . Regarding the plate properties we consider data from Table 1.1 however the thickness is assumed to be on the limit of moderately thick plates with  $h_o/a = 0.1$ , since [17] examines standard and higher-order plate models.

Table 1.6 contains the comparison results against the CPT model in Shufrin & Eisenberger [17]. We can observe that the first two frequencies are predicted with good accuracy, whereas for higher frequencies discrepancies are evident. Table 1.7 contains results concerning the C-C-C-C case with  $\tau_x = 0.25$  for reference, where it is shown that for the standard case a deviation of up to 3% is observed at higher frequencies. Deviations can be attributed to the interpolation scheme based on which the distributed thickness properties are assigned to each element in our solver and also consideration of boundary conditions via augmentation of the system of equations. The C-F-F-F problem is considered challenging and taking into consideration that we compared against another numerical model, the results overall lie within acceptable limits.

Table 1.5: Frequency parameters  $\Omega = \omega a^2 \sqrt{\rho_A(h_o)/D(h_o)}$  for C-C-C-C rectangular plate with taper ratio  $\tau_x = 0.2$  ( $h_o = 0.01m$ ,  $h_1 = 0.012m$ ).

	$\tau_x = 0.2$			$\tau_x = 0.4$		
id	Katsikadelis [15]	Kuttler [16]	DKT (5344)	Katsikadelis [15]	Kuttler [16]	DKT (5344)
$\Omega_1^2$	$0.1553 \cdot 10^4$	$0.1559 \cdot 10^4$	$0.1557 \cdot 10^4$	$0.1827 \cdot 10^4$	$0.1837 \cdot 10^4$	$0.1832 \cdot 10^4$
$\Omega_2^2$	$0.6182 \cdot 10^4$	$0.6443 \cdot 10^4$	$0.6471 \cdot 10^4$	$0.7251 \cdot 10^4$	$0.7605 \cdot 10^4$	$0.7587 \cdot 10^4$
$\Omega_3^2$	$0.6212 \cdot 10^4$	$0.6469 \cdot 10^4$	$0.6483 \cdot 10^4$	$0.7383 \cdot 10^4$	$0.7632 \cdot 10^4$	$0.7630 \cdot 10^4$
$\Omega_4^2$	$0.1390 \cdot 10^5$	$0.1407 \cdot 10^5$	$0.1411 \cdot 10^5$	$0.1639 \cdot 10^5$	-	$0.1664 \cdot 10^5$

The eigenfunction contours are included in Figure 1.7 for comparison purposes against Figure 1.6, where we can observe the effects of linear thickness variation on the nondimensional frequencies and the eigenfunctions. All the above test cases support the validity of the present numerical tool for thin tapered plate analysis.

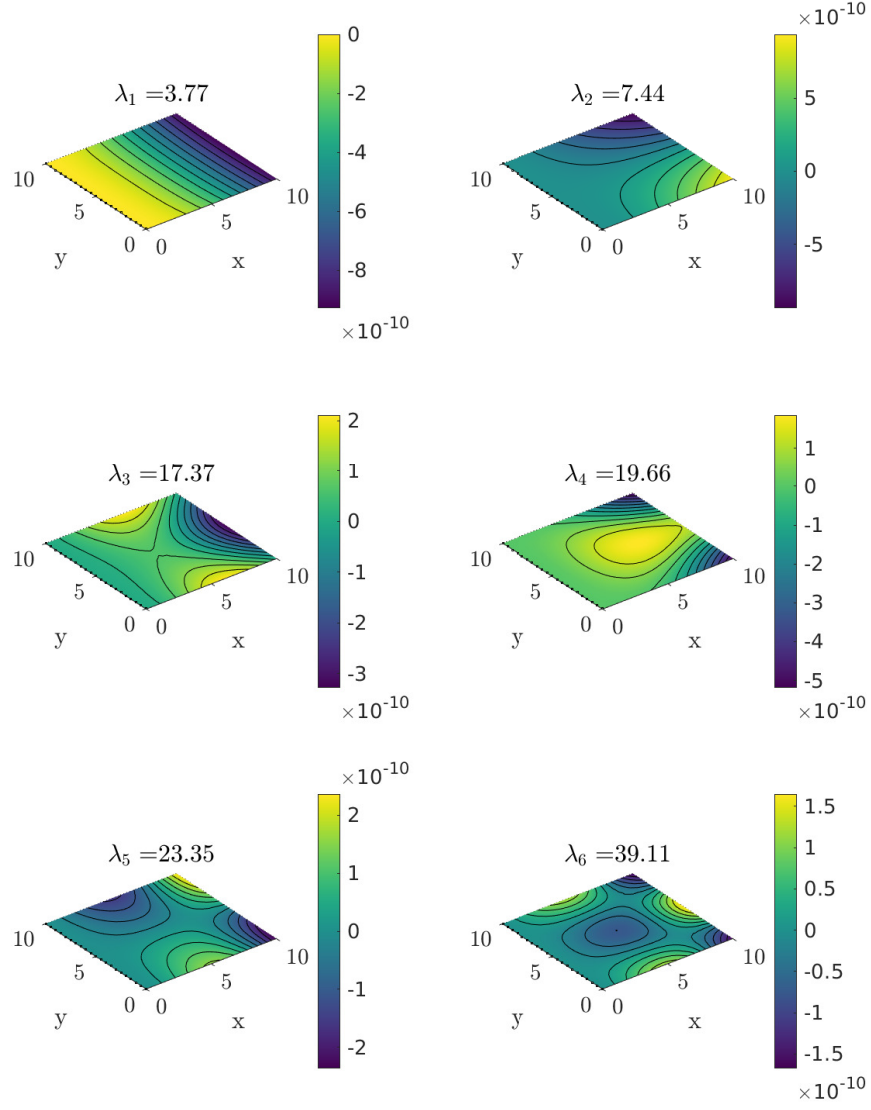


Figure 1.7: Eigenfunction contour plots for C-F-F-F results from Table 1.6 with color bar referring to the  $z$ -coordinate.

Table 1.6: Frequency parameters  $\lambda_s = \omega a^2 \sqrt{\rho h_o / D(h_o)} / \pi^2$  for C-F-F-F rectangular plate with taper ratio  $\tau_x = 0.5$  ( $h_o = 1.0m$ ,  $h_1 = 0.5m$ ). [\[Re-examine\]](#)

id	Shufrin <a href="#">[17]</a>	DKT (5344)	Diff(%)
1	0.3859	0.3816	1.13
2	0.7563	0.7541	0.29
3	1.8485	1.7598	4.79
4	1.9438	1.9924	-2.50
5	2.4184	2.3659	2.17
6	4.0317	3.9625	1.71

Table 1.7: Frequency parameters  $\lambda_s = \omega a^2 \sqrt{\rho h_o / D(h_o)} / \pi^2$  for C-C-C-C rectangular plate with taper ratio  $\tau_x = 0.25$  ( $h_o = 1.0m$ ,  $h_1 = 0.75m$ ). [\[Re-examine\]](#)

id	Shufrin <a href="#">[17]</a>	DKT (5344)	Diff(%)
1	3.1767	3.1630	0.43
2	6.4650	6.3801	1.31
3	6.4782	6.3920	1.33
4	9.5610	9.3505	2.20
5	11.5702	11.2599	2.68
6	11.6375	11.3580	2.40

### 1.3.2 Static response

**Navier solution for S-S-S-S rectangular plate.** Next, the static solution under (i) uniform and (ii) concentrated loading scenarios is considered. For the simply supported plate with constant thickness, numerical results are compared against analytical solutions. Navier solutions for the S-S-S-S rectangular plate case are derived by means of Fourier series representations [\[18\]](#). For the case of uniform load, the plate deflection is expressed as

$$w(x, y) = \frac{16p_0}{D\pi^6} \sum_{n=1,3,5..} \sum_{m=1,3,5..} \frac{\sin(m\pi x)\sin(n\pi y)}{mn(m^2/a^2 + n^2/b^2)^2} \quad (1.42)$$

where  $a, b$  are the  $x$ - and  $y$ -expanded dimensions respectively. For the concentrated load positioned at  $(\xi, \eta)$  the deflection reduces to,

$$w(x, y) = \frac{16p_0}{Dab\pi^6} \sum_{n=1,3,5..} \sum_{m=1,3,5..} \frac{\sin(m\pi\xi/a)\sin(n\pi\eta/b)\sin(m\pi x/a)\sin(n\pi y/b)}{mn(m^2/a^2 + n^2/b^2)^2} \quad (1.43)$$

Setting  $p_o = 100N$  and keeping a large number of terms to ensure convergence, the results for  $(\xi, \eta) = (5, 5)$  are presented in Table 1.8 and Figure below. The plate properties are provided in Table 1.1 and a mesh of  $N_{elem} = 1336$  is considered. Regarding the sign convention of the present formulation, loads and displacements are positive when directed towards the positive  $z$ -axis. The results are in excellent agreement with the analytical solution. The selected test case illustrates that concentrated load conditions lead to higher bending displacement compared to the same load uniformly distributed along the surface of the plate.

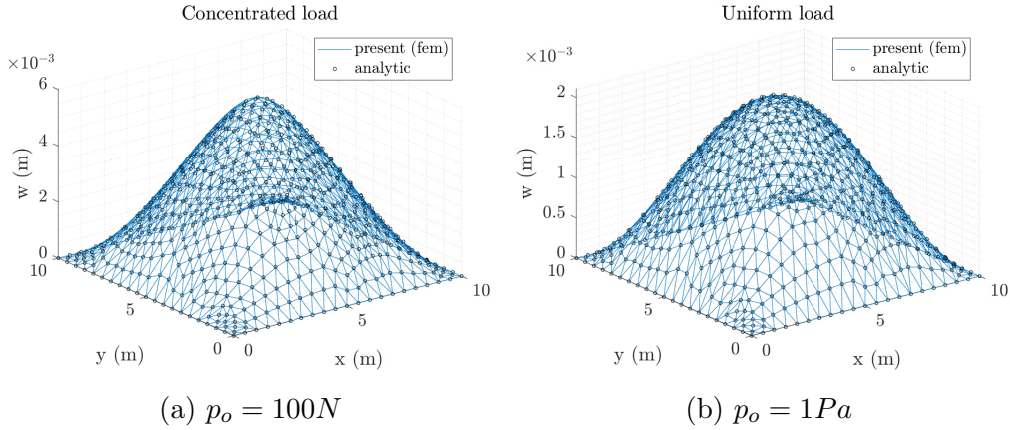


Figure 1.8: Comparison with Navier solution in [18] for S-S-S-S rectangular plate with properties in Table 1.1 under (a) concentrated and (b) uniform load.

Table 1.8: Maximum bending displacement  $w_{max}(m)$  for static load cases.

	Timoshenko [18]	DKT (1336)	Diff(%)
concentrated	$0.6015 \cdot 10^{-2}$	$0.6034 \cdot 10^{-2}$	+0.3070
uniform	$0.2111 \cdot 10^{-2}$	$0.2108 \cdot 10^{-2}$	-0.1427



**Rectangular plate under distributed load.** The following test case is included to verify that the present numerical tool is capable of predicting the bending displacements under distributed load conditions. We compared results obtained with the DKT solver against ANSYS Mechanical 2022 R2 for a rectangular plate with properties shown in Table 1.1 under a distributed load. The load profile is based on the following formula,

$$f_x = \frac{1}{s} \sqrt{2\pi} \exp\left(-0.5[(x-m)/s]^2\right), \quad x, y \in [-1, 1] \quad (1.44)$$

$$x = a \cdot 0.5(1 - x), \quad y = b \cdot 0.5(y + 1)$$

where  $s = 0.2, m = 0.6$  are parameters. The above transformation is used to take into consideration the dimensions of the plate  $a, b$  and its placement in the body-fixed coordinate system, as shown in Figure 1.9.

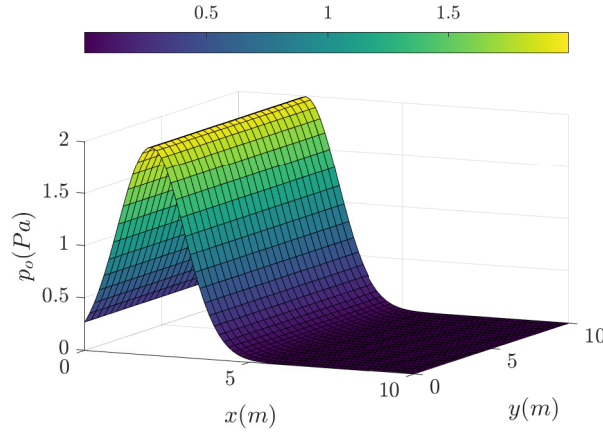


Figure 1.9: Distributed load scenario.

Regarding the examined boundary conditions, we consider the following scenarios: (i) C-F-F-F (clamped along  $x = 0$ ) and (i) F-F-C-F (clamped along  $x = a$ ). Since the load distribution resembles the hydrodynamic loading of a wing that undergoes a prescribed flapping motion, these boundary conditions are of value. The first is motivated from the case of a wing that is actuated from its leading edge, closer to which maximum loading occurs. The latter is motivated from the case of a T-foil, where only the half wing is simulated and the clamped edge corresponds to the position of the T-foil support.

The sign convention in ANSYS Mechanical differs from plateFEM, since negative values of the distributed load yields deformation in the positive of the Z- axis. The mesh in ANSYS consists of 26400 SHELL 181 or SHELL 63 (legacy) elements. The distributed load is imported as tabulated data

using the “External Data” from the “Component Systems” in ANSYS Workbench. It is linked to the Setup. Moreover, in Geometry < Surface Body < Commands (APDL), the following lines can be added to control the plate thickness

```
et, matid, SHELL63
etcontrol, set, on
r, matid, 0.0198
```

Alternatively, we can open the DesignModeller to change the thickness of the plate. Similarly, for the case of tapered plates tabulated data can be imported using “External Data” to incorporate distributed thickness profiles into the analysis.

The static response of the plate due to distributed load is shown in Figure 1.10-1.10 for the F-F-C-F and the C-F-F-F boundary conditions respectively. The maximum bending displacement results are summarized in Table 1.9 where it is evident that boundary conditions play a significant role in the plate’s response.

Table 1.9: Maximum bending displacement  $w_{max}(m)$  for distributed load case.

	ANSYS	DKT (1336)	Diff(%)
C-F-F-F		0.0060	
F-F-C-F		0.0408	

### 1.3.3 Hydrodynamic load excitation

Simulate the response of the optimal thruster with taper ratio? The distributed load corresponds to the solution of the BEM solver for a wing with these geometric dimensions and a NACA0012 section performing a prescribed flapping-motion. At a selected time-instance, we stored the hydrodynamic load data and used it for the FEM static analysis.

## 1.4 Discussion and future extensions

Regarding the analysis of tapered plates under hydrodynamic load excitation, we could also focus on investigate effects of various wing configurations in terms of boundary conditions, relating to engineering applications of

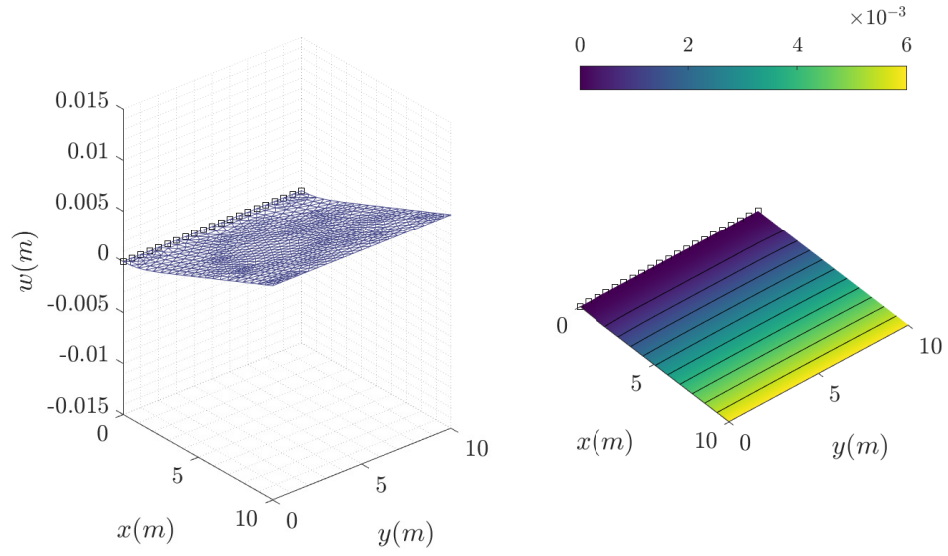


Figure 1.10: Bending displacement [left] and contour [right] for the C-F-F-F plate under distributed load.

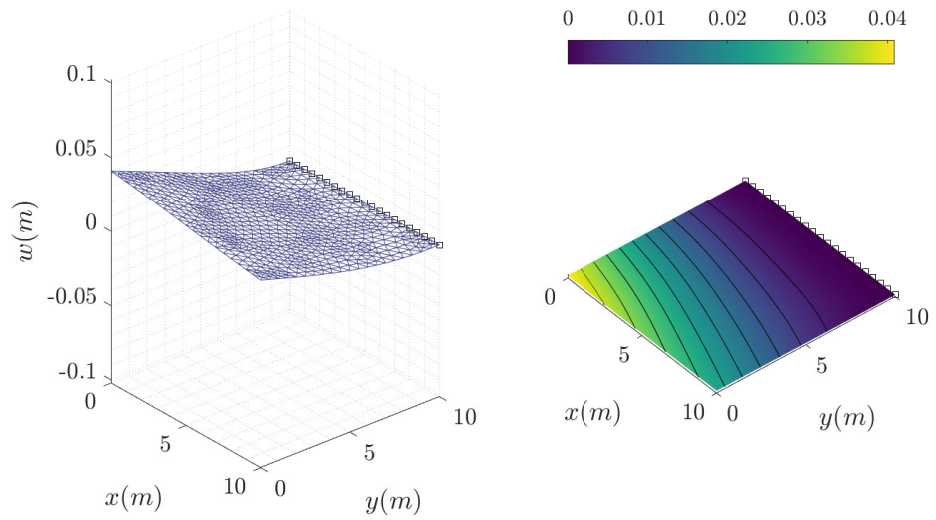


Figure 1.11: Bending displacement [left] and contour [right] for the F-F-C-F plate under distributed load.

biomimetic wing thrusters, (i) on natural frequencies and (ii) wing response under static loads.

The following aspects can be addressed to improve the accuracy of the present finite element scheme:

- Instead of using a function for scattered data interpolation, the DKT interpolation scheme that is used for field variables  $(\phi, \beta_x, \beta_y)$  can also be exploited for distributed load and thickness data assignment to the mesh.
- Additional damping terms can be included to the modelling.
- Parallel computation on graphics cards, such as the the cuSPARSE() functions from CUDA, can be exploited to decrease the computational time.

All the above implementation are direct and can be addressed with relative ease. Future extensions that are considered more demanding, yet open the field of future applications of the present numerical tool, include the following:

- Higher-order plate theory formulations which are suitable for moderately thick plates with  $h/a$  of the order of 0.1
- Sandwich plate (core, facings) formulation based on CPT, see, e.g. Wang [11]
- Perform fluid-structure simulations for flexible plates via coupling the present finite element model with viscous CFD to obtain improved predictions for the response in cases where viscous phenomena are dominant.

# Bibliography

- [1] IMO, “Marine environmental protection committee. Revised IMO strategy on reduction of GHG emissions from ships, resolution MEPC.377 (80). MEPC 80/WP.12 annex 11 International Maritime Organization,” 2023. [Online]. Available: <https://www.imo.org/en/MediaCentre/PressBriefings/pages/Revised-GHG-reduction-strategy-for-global-shipping-adopted-.aspx>.
- [2] J. Faber and S. H. et al., “Fourth IMO greenhouse gas study,” *International Maritime Organization*, 2020. [Online]. Available: <https://www.imo.org/en/ourwork/Environment/Pages/Fourth-IMO-Greenhouse-Gas-Study-2020.aspx>.
- [3] K. V. Rozhdestvensky and V. A. Ryzov, “Aerodynamics of flapping-wing propulsors,” *Progress in Aerospace Sciences*, vol. 39, pp. 585–633, 2003. DOI: [https://doi.org/10.1016/S0376-0421\(03\)00077-0](https://doi.org/10.1016/S0376-0421(03)00077-0).
- [4] W. Shyy, H. Aono, S. Chimakurthi, *et al.*, “Recent progress in flapping wing aerodynamics and aeroelasticity,” *Engineering Analysis with Boundary Elements*, vol. 46, pp. 284–327, 7 2014.
- [5] R. K. Katzschmann, “Building and controlling fluidically actuated soft robots: From open loop to model-based control,” Ph.D. dissertation, Department of Mechanical Engineering MIT, 2018.
- [6] K. Belibassakis, E. Filippas, and G. Papadakis, “Numerical and experimental investigation of the performance of dynamic wing for augmenting ship propulsion in head and quartering seas,” *Journal of Marine Science and Engineering*, vol. 10, no. 1, 2022. DOI: [10.3390/jmse10010024](https://doi.org/10.3390/jmse10010024).
- [7] D. Ntouras, G. Papadakis, and K. Belibassakis, “Ship bow wings with application to trim and resistance control in calm water and in waves,” *Journal of Marine Science and Engineering*, vol. 10, no. 4, 2022. DOI: [10.3390/jmse10040492](https://doi.org/10.3390/jmse10040492).

- [8] Q. Zhu, “Numerical simulation of a flapping foil with chordwise or span-wise flexibility,” *AIAA*, vol. 45, pp. 2448–2457, 10 2007. DOI: <https://doi.org/10.2514/1.28565>.
- [9] H. Dai, H. Luo, P. J. S. A. F. de Sousa, and J. F. Doyle, “Thrust performance of a flexible low-aspect-ratio pitching plate,” *Physics of Fluids*, vol. 24, p. 101903, 2012. DOI: <http://dx.doi.org/10.1063/1.4764047>.
- [10] O. Zienkiewicz and R. Taylor, *The Finite Element Method for Solid and Structural Mechanics*. Elsevier, 2005.
- [11] C. Wang, J. Reddy, and K. Lee, *Shear Deformable Beams and Plates. Relationships with Practical Solutions*. Elsevier, 2000.
- [12] J.-L. Batoz, K. Bathe, and L. Ho, “A study of three-node triangular plate bending elements,” *International Journal for Numerical Methods in Engineering*, vol. 15, pp. 1771–1812, 1980.
- [13] F. Paraz, C. Eloy, and L. Schouveiler, “Experimental study of the response of a flexible plate to a harmonic forcing in a flow,” *Comptes Rendus Mèchanique*, vol. 342, no. 9, pp. 532–538, 2014.
- [14] A. W. Leissa, “The free vibration of rectangular plates,” *Journal of Sound and Vibration*, vol. 31, pp. 257–293, 3 1973. DOI: [https://doi.org/10.1016/S0022-460X\(73\)80371-2](https://doi.org/10.1016/S0022-460X(73)80371-2).
- [15] J. T. Katsikadelis and E. J. Sapountzakis, “A bem solution to dynamic analysis of plates with variable thickness,” *Computational Mechanics*, vol. 7, pp. 369–379, 1991. DOI: <https://doi.org/10.1007/BF00350166>.
- [16] J. R. Kuttler and V. G. Sigillito, “Vibrational frequencies of clamped plates of variable thickness,” *Journal of Sound and Vibration*, vol. 86, pp. 181–189, 2 1983. DOI: [https://doi.org/10.1016/0022-460X\(83\)90747-2](https://doi.org/10.1016/0022-460X(83)90747-2).
- [17] I. Shufrin and M. Eisenberger, “Vibration of shear deformable plates with variable thickness — first-order and higher-order analyses,” *Journal of Sound and Vibration*, vol. 290, pp. 465–489, 2006. DOI: [doi:10.1016/j.jsv.2005.04.003](https://doi.org/10.1016/j.jsv.2005.04.003).
- [18] S. Timoshenko and S. Woinowsky-Krieger, *Theory of Plates and Shells*. McGraw-Hill, 1959.